

Electronic and Mechanical Properties of Graphene–Germanium Interfaces Grown by Chemical Vapor Deposition

Brian Kiraly,^{†,‡} Robert M. Jacobberger,[§] Andrew J. Mannix,^{†,‡} Gavin P. Campbell,[†] Michael J. Bedzyk,^{†,||} Michael S. Arnold,[§] Mark C. Hersam,^{*,†,⊥} and Nathan P. Guisinger^{*,‡}

[†]Department of Materials Science and Engineering, Northwestern University, Evanston, Illinois 60208, United States

[‡]Center for Nanoscale Materials, Argonne National Laboratory, Argonne, Illinois 60439, United States

[§]Department of Materials Science and Engineering, University of Wisconsin-Madison, Madison, Wisconsin 53706, United States

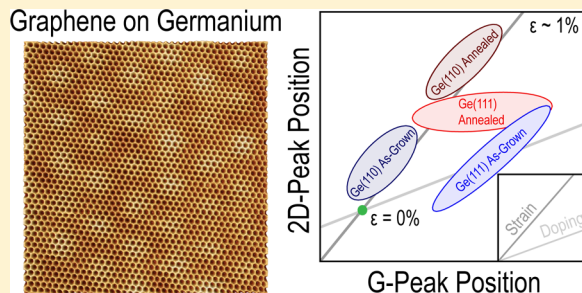
^{||}Department of Physics and Astronomy, Northwestern University, Evanston, Illinois 60208, United States

[⊥]Department of Chemistry, Northwestern University, Evanston, Illinois 60208, United States

Supporting Information

ABSTRACT: Epitaxially oriented wafer-scale graphene grown directly on semiconducting Ge substrates is of high interest for both fundamental science and electronic device applications. To date, however, this material system remains relatively unexplored structurally and electronically, particularly at the atomic scale. To further understand the nature of the interface between graphene and Ge, we utilize ultrahigh vacuum scanning tunneling microscopy (STM) and scanning tunneling spectroscopy (STS) along with Raman and X-ray photoelectron spectroscopy to probe interfacial atomic structure and chemistry. STS reveals significant differences in electronic interactions between graphene and Ge(110)/Ge(111), which is consistent with a model of stronger interaction on Ge(110) leading to epitaxial growth. Raman spectra indicate that the graphene is considerably strained after growth, with more point-to-point variation on Ge(111). Furthermore, this native strain influences the atomic structure of the interface by inducing metastable and previously unobserved Ge surface reconstructions following annealing. These nonequilibrium reconstructions cover >90% of the surface and, in turn, modify both the electronic and mechanical properties of the graphene overlayer. Finally, graphene on Ge(001) represents the extreme strain case, where graphene drives the reorganization of the Ge surface into [107] facets. From this work, it is clear that the interaction between graphene and the underlying Ge is not only dependent on the substrate crystallographic orientation, but is also tunable and strongly related to the atomic reconfiguration of the graphene–Ge interface.

KEYWORDS: Epitaxy, surface reconstruction, chemical vapor deposition, scanning tunneling microscopy, scanning tunneling spectroscopy, Raman spectroscopy



Chemical vapor deposition of graphene on metal foils enabled the rapid development of fundamental research and diverse, scalable applications utilizing the unique optical, mechanical, and electronic properties of graphene.^{1–4} Studies of graphene growth subsequently burgeoned with demonstrations on alternate substrates,^{5–7} with novel precursors,^{8–11} and under a variety of atmospheric conditions.^{12–17} Most recently, graphene was directly grown on semiconducting Ge surfaces, marking a significant departure from conventional metallic systems and another step toward graphene-based applications in electronics.^{18,19} Lee et al. further utilized the inherent asymmetry of crystalline Ge surfaces to control the orientation of the graphene overlayer, leading to epitaxially oriented, wafer-scale graphene.¹⁹ While this work identified suitable growth conditions for epitaxial graphene directly on a semiconducting surface, the structure and properties of the resulting material interface remain relatively unexplored, particularly at the atomic scale.

Since its initial isolation,^{20–22} numerous studies have shown that the interfaces between graphene and its surroundings can have a significant impact on both the observed properties of graphene itself and the composite properties of the system.^{23–30} For example, carrier transport in graphene is strongly influenced by the local dielectric environment, with atomically pristine interfaces enabling observations of correlated electron–electron effects,^{31,32} fractal band structure in graphene superlattices,^{33,34} and topological valley currents.³⁵ Furthermore, van der Waals (vdW) forces at 2D interfaces often result in mutual strain in the atomic lattices. Such strain can alter electronic properties,^{36,37} induce both variant and nonvariant Gauge fields,^{38,39} and modify chemical properties.⁴⁰ As graphene is incorporated into increasingly complex

Received: July 17, 2015

Revised: September 25, 2015

Published: October 27, 2015



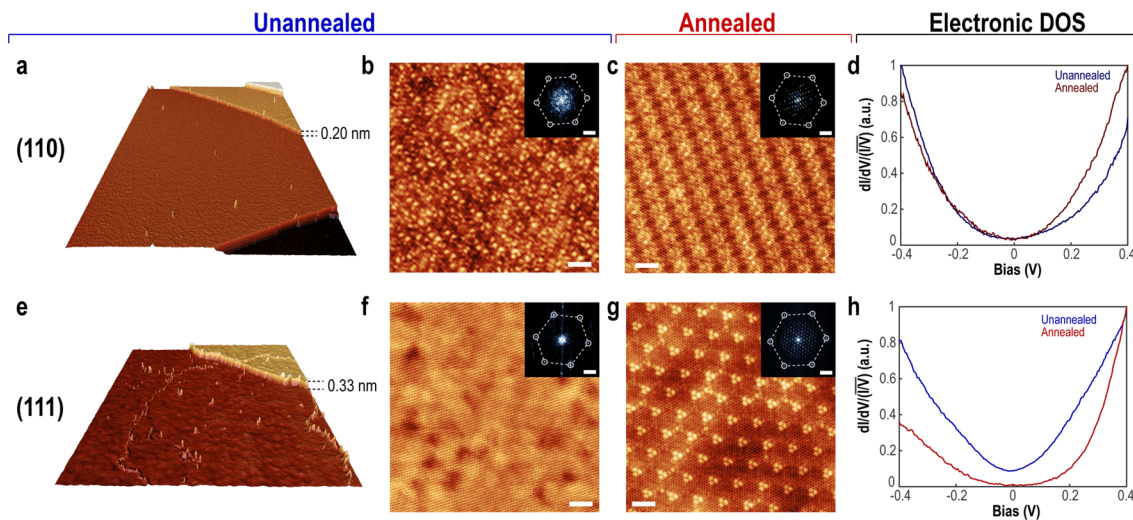


Figure 1. (a) Large scale STM image of graphene on Ge(110) (size: 500 nm × 310 nm, $V = 2$ V, $I = 100$ pA). (b) Atomically resolved graphene lattice on top of a disordered Ge(110) terrace (scale bar = 2 nm, $V = 1.4$ V, $I = 80$ pA). Inset: Fourier transform (FT) of image in (b) with hexagonal symmetry of graphene overlaid (scale bar = 2 nm $^{-1}$). (c) Atomically resolved graphene lattice observed over the top of the ordered 1D reconstruction of the Ge(110) surface after vacuum annealing (scale bar = 2 nm, $V = -1$ V, $I = 400$ pA). Inset: Fourier transform (FT) of image in (c); the highlighted hexagonal symmetry is due to graphene lattice with additional symmetry attributed to underlying Ge (scale bar = 2 nm $^{-1}$). (d) Normalized differential tunneling conductance spectra of the graphene/Ge(110) system both before (blue) and after (red) vacuum annealing. (e) Large scale STM image of graphene on Ge(111) (size: 200 nm × 163 nm, $V = -1$ V, $I = 100$ pA). (f) Atomically resolved graphene on top of the disordered Ge(111) terrace with vertical corrugation <50 pm (scale bar = 2 nm, $V = -0.2$ V, $I = 100$ pA). Inset: Fourier transform (FT) of image in (f), again with graphene reciprocal lattice highlighted (scale bar = 2 nm $^{-1}$). (g) Atomically resolved graphene lattice observed over the top of the ordered close-packed reconstruction of the Ge(111) surface after vacuum annealing (scale bar = 2 nm, $V = 0.4$ V, $I = 100$ pA). Inset: Fourier transform (FT) of image in panel (g) demonstrating 6-fold symmetry in both the graphene and underlying Ge (scale bar = 2 nm $^{-1}$). (h) Normalized differential tunneling conductance spectra of the graphene/Ge(111) system both before (blue) and after (red) vacuum annealing demonstrating a transformation from quasi-free-standing graphene (blue) to strongly interacting graphene (red).

heterogeneous vdW solids, strain and related interfacial properties will assume a significant role in the functionality and performance of these systems. As such, a thorough understanding of graphene interfaces must be developed to facilitate future technologies.

In this work, atomic-scale scanning tunneling microscopy (STM), Raman spectroscopy, and X-ray photoelectron spectroscopy (XPS) are utilized to characterize graphene grown on Ge(111), Ge(110), and Ge(001). Scanning tunneling spectroscopy (STS) reveals significant electronic interaction between graphene and the Ge(110) surface, yet nearly complete electronic isolation between graphene and the Ge(111) surface. This result is consistent with the previous observation of epitaxy on Ge(110) and rotational disorder on Ge(111).¹⁹ From both STM and Raman spectroscopy, it is clear that strain is persistent in the as-grown samples and plays a central role in determining composite properties. Specifically, we utilize this intrinsic strain to tailor properties of Ge/graphene via vacuum annealing. Using this approach, the graphene overlayer stabilizes previously unreported Ge(110) and Ge(111) surface reconstructions. Despite their strongly overlapping electronic density of states (DOS), Raman spectroscopy and XPS confirm that the Ge reconstructions and graphene lattice do not chemically bond. The reconstructions, in turn, modify the properties of the graphene by inducing an increase in compressive strain in the graphene on Ge(110) and facilitating charge transfer in the Ge(111)/graphene system. Overall, this work shows that the crystallographic orientation of the germanium substrate plays a significant role in both the growth behavior and resulting interfacial properties of the composite system.

Graphene was grown on Ge(001), Ge(110), and Ge(111) by chemical vapor deposition (CVD) of CH₄ in H₂ and Ar at atmospheric pressure; further information on the Ge surface preparation and growth can be found in the [Supporting Information](#). Previous work has shown that a single crystallographic orientation of graphene can be achieved on Ge(110) at low CH₄ partial pressure but that two orientations are obtained at higher CH₄ partial pressure.¹⁹ To study both epitaxial orientations, the latter condition was used. Low-energy electron diffraction (LEED) confirms that the resulting graphene on Ge(110) contains two rotational domains misaligned by 30° ([Figure S1a](#)).¹⁹ Graphene on Ge(111) also demonstrates two preferential domain orientations; however, one of the domains exhibits increased rotational freedom leading to a Gaussian distribution of domain orientations centered about the first domain ([Figure S1b,d,e](#)). Interestingly, the second domain is rotated 30° from the first and contains very little rotational spread, similar to Ge(110) ([Figure S1a](#)), suggesting that epitaxial domain registry between graphene nuclei and the Ge surfaces occurs for both the (110) and (111) surfaces.

The as-grown graphene/Ge samples were studied with STM to understand the atomic nature of the graphene/Ge interface. Before imaging, the samples were brought under UHV and degassed at ~400 °C (to remove physisorbed species introduced during exposure to atmosphere), a process which possibly induces some morphological changes in the atomic Ge structure compared with the pristine postgrowth product. Large-scale STM images of the graphene-covered Ge(110) and Ge(111) surfaces are shown in [Figure 1a,e](#), respectively. The nominally as-grown surfaces possess atomic terraces separated by steps characteristic of clean Ge surfaces prepared in UHV.^{41,42} The presence of steps and terraces ([Figure 1a,e](#))

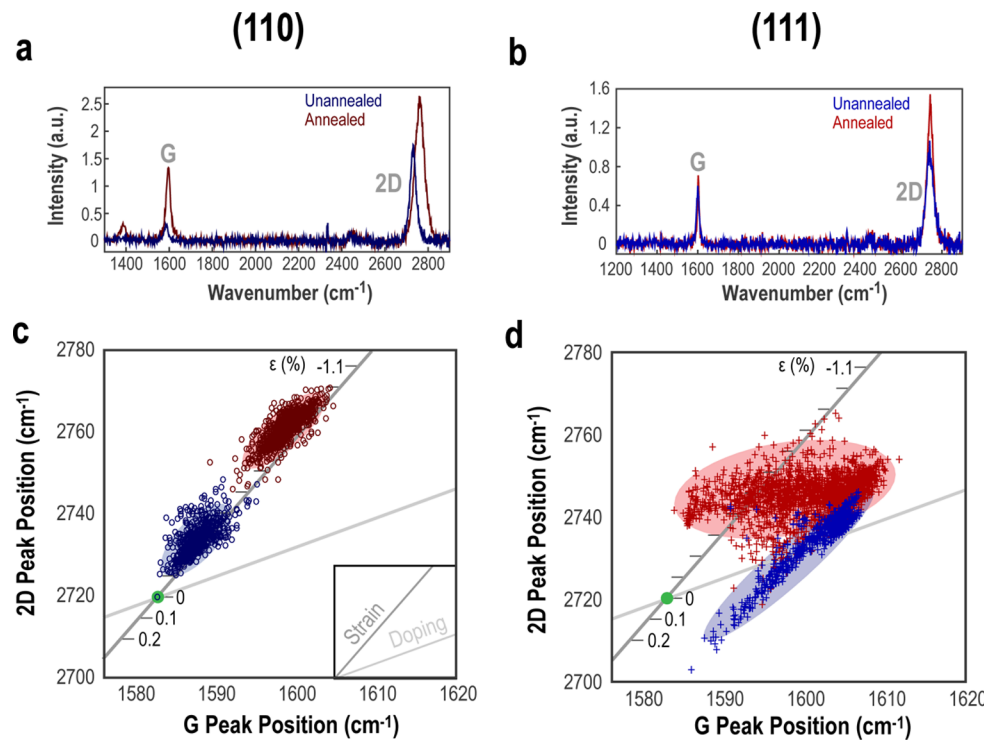


Figure 2. (a) Raman spectra of graphene on Ge(110) before (blue) and after (red) annealing. The prominent spectral features for graphene, the G and 2D bands, shift in both position and amplitude after vacuum annealing. (b) Raman spectra of graphene on Ge(111) before (blue) and after (red) annealing. (c) Plot of Raman 2D peak position versus G peak position for spatially resolved Raman spectra of graphene on Ge(110) before (blue) and after (red) vacuum annealing. Shaded circles indicate 95% confidence intervals. (Inset) Gray lines highlight vector decomposition of external effects on the pristine graphene Raman signature. Shifts along the dark gray lines are associated with strain in the graphene lattice, while shifts along the light gray line are associated with variations in carrier doping. (d) Plot of Raman 2D peak position versus G peak position for spatially resolved Raman spectra of graphene on Ge(111) before (blue) and after (red) vacuum annealing.

confirm that graphene acts as a diffusion barrier to ambient contaminants, as similarly prepared bare Ge exposed to ambient conditions possesses a much rougher disordered surface morphology (Figure S2). Despite morphological similarities between the graphene-covered Ge surfaces and pristine UHV-prepared Ge surfaces, notable differences include the observation of partial-steps (Figure S3), which are not observed on bare Ge surfaces, and a general lack of in-plane order underneath the graphene (Figure 1b,f). The stabilization of Ge terraces with half-step heights indicates that the graphene modifies the properties of pristine Ge surfaces, enabling the observation of novel structural motifs.

Simultaneous atomic-scale STM characterization of graphene and its underlying substrate has been demonstrated on Si,⁴³ SiC,⁴⁴ SiO₂,⁴⁵ h-BN,^{46,47} and other semiconductors⁴⁸ to gain valuable insight into these composite systems. Atomically resolved images of graphene on Ge(110) (Figure 1b) and Ge(111) (Figure 1f) show the pristine hexagonal lattice of the graphene superimposed on the disordered backgrounds of the underlying Ge substrates (see Fourier transform (FT) insets Figure 1b,f). Possible explanations for the apparent substrate disorder include quenching of high-temperature disorder upon fast-cooling after growth or restructuring during UHV processing. For example, the vacuum degassing procedure may disrupt the idealized H-passivation model of the underlying Ge proposed by Lee et al.¹⁹ While both surfaces lack order underneath the graphene, quantitative differences exist in their in-plane and out-of-plane structure. Relatively sharp in-plane features (lateral extent < 1 nm) decorate Ge(110) (Figure 1b), often overlapping with the graphene

DOS and resulting in observed vertical corrugations of >150 pm. The Ge(111) surface (Figure 1f), however, displays reduced topographic variation (<50 pm) concomitant with a reduction in electronic inhomogeneity in the graphene (Figures 1h and S4). The structural dissimilarities between the two surfaces are reminiscent of graphene on SiO₂ compared to h-BN,^{47,49} where significant differences in both charge homogeneity and vertical corrugation at the atomic scale translate to modified electronic transport and optical properties.^{24,50,51} The observed structural differences also affect the shape of the energy-dependent graphene DOS (blue curves, Figure 1d,h), where the reduced curvature on Ge(111) indicates a significant decoupling from the underlying substrate. The weakened graphene–substrate interaction on Ge(111) helps elucidate the rotational disorder observed during growth.

Upon vacuum annealing to 700 °C, both the Ge(110) and Ge(111) surfaces restructure into domains demonstrating in-plane ordering underneath the graphene (Figure 1c,g). Topographic STM data and *ex situ* spectroscopic analysis (Figures 2 and 3) indicate that the formation of these domains does not lead to any chemical interaction between the graphene and underlying Ge. The domains formed on the Ge(110) surface possess a previously unidentified 2-fold symmetry and are observed in two orientations at 70° from one another. As seen in Figure 1c, the lattice vector (inter-row spacing) of the linear reconstruction is nearly an order of magnitude larger (1.96 nm) than the hexagonal lattice vector of the overlying graphene (0.246 nm). The reconstructed domains underneath the graphene on the Ge(111) surface have not been observed on bulk Ge(111) substrates. The 6-fold symmetry of the

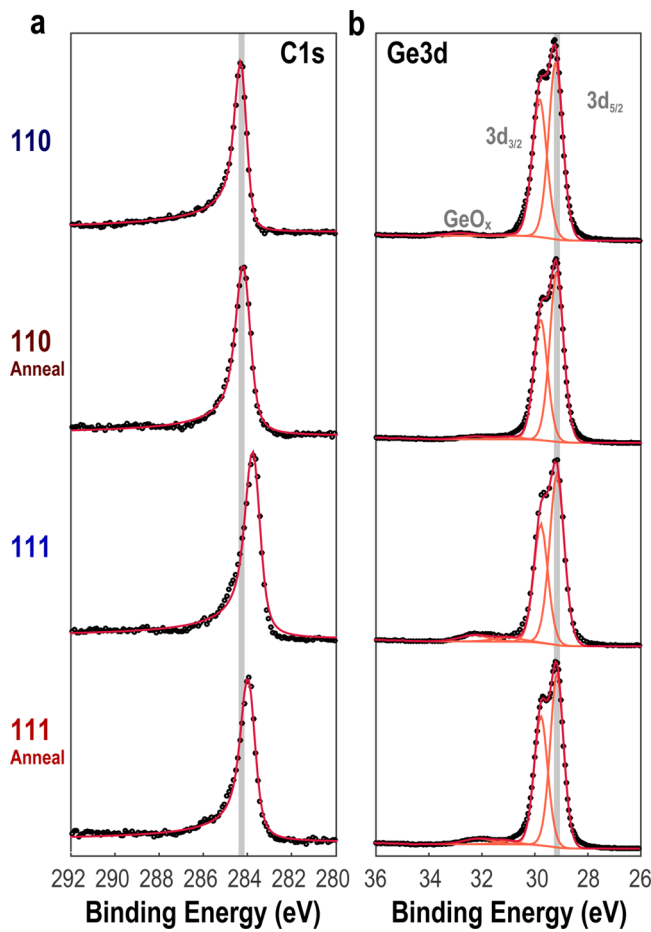


Figure 3. (a) C 1s XPS spectra taken from the Ge(110)/graphene and Ge(111)/graphene samples before and after annealing, with raw data (black) fitted with a Doniach–Sunjic profile (red) vertically offset for clarity. (b) Ge 3d XPS spectra taken from the Ge(110)/graphene and Ge(111)/graphene samples before and annealing. Raw data (black) is fitted with symmetric Voigt peaks (orange) centered at energies 29.3, 29.9, and 32.3 for Ge 3d_{5/2}, Ge 3d_{3/2}, and GeO_x, respectively. The sum of the individual peaks is shown in red.

reconstruction on the Ge(111) surface (Figure 1g) is unlike the conventional c(2 × 8) reconstruction of Ge(111), in which the intrinsic 6-fold symmetry is broken into triply degenerate 2-fold symmetry (Figure S5). The reconstructed regions further deviate in behavior from clean surfaces in that they appear to grow in lateral extent with increased thermal processing, leading to coverages from <20% to 100%. The growth and union of reconstructed domains deviate from the behavior of most common semiconductor surface reconstructions, which are typically observed uniformly over the entire surface. Finally, STM analysis indicates that the reconstructed Ge surfaces survive ambient exposure. The emergence and stability of unidentified substrate reconstructions further reinforces the conclusion that the graphene overlayer modifies the energetic landscape of the underlying Ge.

Tunneling point spectroscopy reveals that the formation of ordered Ge reconstructions has orientation-dependent effects on the electronic density of states (DOS) of graphene. As seen in the preannealing and postannealing curves in Figure 1d, the DOS of the Ge(110)/graphene surface is not strongly affected by the 700 °C vacuum annealing procedure. The parabolic nature of the DOS bands points to a strong electronic

interaction between the graphene and the underlying Ge surface corresponding to a reduction in the graphene Fermi velocity, supporting the model of interaction/epitaxy between the two material surfaces.¹⁹ Contrary to the Ge(110) surface, the Ge(111)/graphene interface is strongly affected by vacuum annealing. Before annealing, the graphene demonstrates a highly linear DOS in the vicinity of the Fermi energy (E_F) (Figure 1h, blue curve), resembling quasi-freestanding graphene. Furthermore, the location of E_F with respect to the Dirac point (E_D) is highly homogeneous, indicating that the charge variation is of the same order as graphene on h-BN (Figure S4). This quasi-freestanding electronic behavior is drastically altered upon vacuum annealing to ~700 °C. The postannealed (red) curve in Figure 1h shows a similar parabolic structure to the graphene on Ge(110), signaling a transition from nearly noninteracting to strongly interacting following annealing. The charge homogeneity on Ge(111) and electronic interaction on Ge(110) before annealing are further elucidated in the Raman data (Figure 2), which enables the concurrent examination of electronic and mechanical properties through vibrational spectroscopy.

To further characterize the interfacial properties in these systems, spatially resolved Raman spectroscopy was utilized to probe variations in the graphene vibrational structure on Ge. Representative point spectra from unannealed graphene on Ge(110) and Ge(111) are shown in blue in Figure 2a,b, respectively. The 2D and G bands are visible at 2720–2770 and 1580–1605 cm⁻¹, respectively. Plots of the 2D versus G peak positions for Raman spectra taken over 100–1600 μm² areas on the as-grown Ge/graphene surfaces are shown in blue in Figure 2c,d, with corresponding maps given in Figures S6 and S7. Utilizing a graphite standard reference (Figure S8), we conservatively estimate the accuracy of the peak position to be within 2 cm⁻¹. As noted in ref 52, contributions from strain and charge doping can be deconvoluted using vector decomposition within the 2D/G 2-space using suspended monolayer graphene as the origin (green dot in Figure 2c,d). This analysis reveals that both of the as-grown graphene on Ge(110) and Ge(111) samples exhibit relatively significant strain variation across the surface. Utilizing 95% confidence intervals (shaded ovals, Figure 2c,d) the native compressive strain in the graphene on Ge(110) is characterized as $-0.43\% < \epsilon < -0.10\%$. The graphene on Ge(111) exhibits significantly larger strain variation ($\sigma_\epsilon = 0.79\%$) symmetrically around $\epsilon = 0\%$ but also shows a spatially invariant carrier doping level of $n \approx 10^{12} \text{ cm}^{-2}$ (blue data, Figure 2d).⁵² Rotational disorder between the graphene and Ge(111) surface likely contributes to the increased strain variation in the as-grown samples.

As expected from the STM/STS data, the peak position and amplitude of both the 2D and G peaks are affected by vacuum annealing (red curves, Figure 2a,b). The variation in the 2D versus G peaks (red curves, Figure 2c,d) indicates that annealing the two surfaces yields strikingly contrasted results: namely, the Ge(110)/graphene undergoes further compressive strain, whereas the Ge(111) surface shifts from predominantly strain variant to doping variant. As seen in the red confidence interval in Figure 2c for the Ge(110) surface, the variation of compressive strain in the graphene remains comparable to the unannealed sample, whereas the absolute strain increases to $-0.60\% < \epsilon < -0.94\%$. The maps in Figure S7 succinctly illustrate both the unchanged homogeneity and increased strain in the annealed graphene/Ge(110) system. Furthermore, Figure S7e,f clearly shows an inverse relationship between the

strain magnitude and 2D/G area ratio. It is clear that the development of Ge(110) surface reconstructions upon *in situ* annealing directly corresponds to a subsequent increase in the net compressive strain in the graphene. The significant shift in slope of the graphene/Ge(111) data after annealing (red data in Figure 2d), in addition to a sizable broadening of the G-band fwhm and decrease in the 2D/G area ratio (Figure S9), indicates a fundamental shift from spatially varying strain in the as-grown samples to spatially varying charge doping in the annealed samples. Once again, this conclusion is corroborated via the mapping data in Figure S6, where a strong suppression in 2D band variation is observed after annealing. The shift toward charge variation echoes the STM/STS data in which the electronic interaction at the Ge(111)/graphene interface drastically increases after annealing.

Correlating Raman spectra with atomic-scale STM provides unique insight into the mechanical and electronic properties of the Ge/graphene interface, but does not explicitly address the chemical nature of the interface. To address this issue, we utilize X-ray photoelectron spectroscopy (XPS) to directly probe both the presence and bonding state of various elements at the interface. Figure 3a shows the C 1s spectra for the four sets of graphene samples, which include both the Ge(110) and Ge(111) surfaces before and after annealing. All of the C 1s spectra were fit using the Doniach–Sunjic profile for metallic surfaces, reproducing the asymmetric profile characteristic of graphite and graphene.⁵³ The fitted singularity index α of 0.15 is consistent with previous reported values for the case of graphite by Wertheim and Cheung.^{54,55} The XPS spectra confirm that C present in the system is isotropically sp^2 bonded. Furthermore, shifts in the C 1s peak position between the Ge(110) and Ge(111) samples are consistent with the doping observed in the Raman spectroscopy. The Ge 3d peak displays similarly pure chemical characteristics, with all samples showing the characteristic $3d_{5/2}$ and $3d_{3/2}$ doublet of elemental germanium. A minor GeO_x peak is present in the Ge(111) samples, pointing to a minor degree of surface oxidation likely due to the presence of grain boundaries in the graphene. Significantly, all spectra show an absence of Ge–C bonds, confirming the chemical integrity of the graphene before and after annealing.

To further understand the fundamental role of the Ge crystallographic orientation on graphene growth and properties, we studied graphene grown on Ge(001) with STM, STS, Raman, and XPS. The graphene-covered Ge(001) surface (Figure 4a) exhibits a unique, highly faceted topology underneath the graphene monolayer. The faceting primarily occurs along the (107) plane of the Ge and can be strongly affected by cooling procedures used after growth. Despite the relatively significant mass transfer during this process, the growth and structural integrity of the overlying graphene remains uncompromised. In Figure 4b, a coherent graphene lattice is seen stretched across one such facet, illustrating the continuity of the graphene lattice over the relatively large vertical feature. Raman spectroscopy and STM/STS reveal significant variation in both strain and doping of the graphene across this inhomogeneous substrate. Unique to the graphene/Ge(001) system, this substantial mass transport results in the most extreme effects of strain at the graphene/Ge interface.

Despite the extended vertical range of the faceted Ge(001) surface, it also reconstructs upon vacuum annealing. Specifically, the primary effect of the annealing is to flatten the surface, leading to regions of both smaller scale faceting and atomically

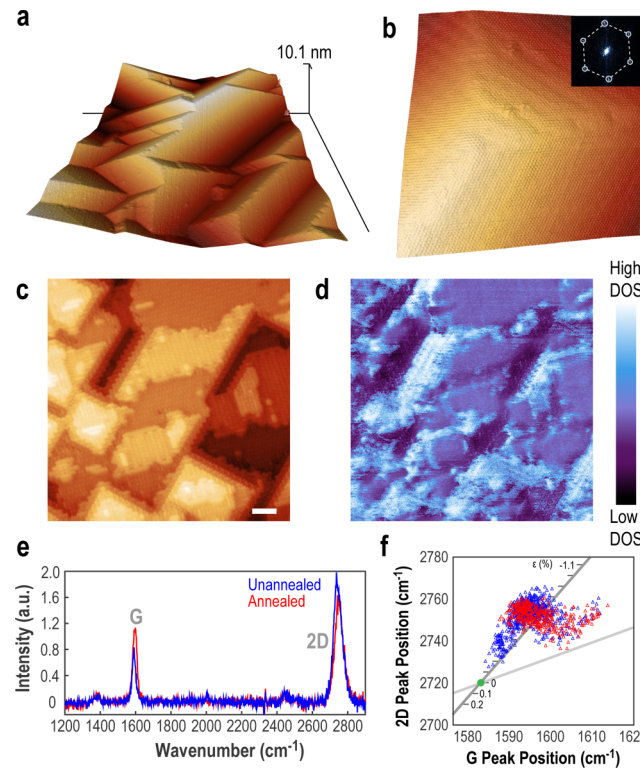


Figure 4. (a) Large scale STM image of graphene on Ge(001) showing significant surface restructuring (size: 200 nm × 142 nm, $V = 2$ V, $I = 200$ pA). (b) Atomically resolved graphene lattice on top of Ge(001) facet with Ge(107) sidewalls (size: 18 nm × 18 nm, $V = 0.2$ V, $I = 800$ pA). Inset: Fourier transform (FT) of image in (b) highlighting reciprocal graphene lattice. (c) Flat domain of reconstructed Ge(001) surface observed after vacuum annealing (scale bar = 4 nm, $V = -1$ V, $I = 800$ pA). (d) STS plot of electronic DOS near E_F illustrating significant variation correlated with underlying features of the Ge(001) surface. (e) Representative Raman spectra of graphene on Ge(001) before (blue) and after (red) annealing. (f) Plot of 2D peak position versus G peak position for spatially resolved Raman spectra from graphene on Ge(001).

flat terraces (Figure S10). One flat area, shown in Figure 4c, demonstrates a similar reconstruction to Ge(001)-2 × 1, which is observed on pristine UHV-prepared surfaces. The structures share similar rectangular symmetry and 90° rotational alignment between subsequent steps; however, the observed surface has a 3 × 2 unit cell. The 700 °C vacuum annealing also has a significant impact on the electronic properties of the graphene/Ge(001) interface, causing the enhancement of spatial inhomogeneities in the electronic DOS of the graphene (Figure 4d). Finally, as with all Ge surfaces, vacuum annealing on the Ge(001) surface does not impact the structural integrity of the graphene.

Raman spectra from the graphene/Ge(001) system qualitatively resemble the other two surfaces. The 2D and G modes are readily identifiable with a nearly undetectable D band peak (Figure 4e). Plotting the 2D versus G peak positions in Figure 4f, it is clear that while subsets of the data resemble strain variation in the graphene, it is difficult to unambiguously deconvolute the effects of strain and doping as in Figure 2c,d. Raman maps of the G and 2D peak positions (Figure S11) indicate that significant point-to-point variation is responsible for the relative spread of data in Figure 4f. This variation is almost certainly related to the inhomogeneous topography and

electronic landscape of the Ge(001) surface. It is noteworthy, however, to point out that the Raman spectra of the graphene are relatively unchanged by vacuum annealing, which is a property unique to the Ge(001) surface.

In conclusion, we confirm a significant difference in substrate interaction between as-grown graphene on Ge(110) and Ge(111), consistent with previous models proposed to explain the difference in graphene epitaxy between these two substrate crystallographic orientations. Furthermore, Raman spectroscopy reveals strain variations up to 1% (0.4%) across the as-grown graphene samples on Ge(111) (Ge(110)), with relatively minimal charge fluctuation. Thermal processing of these systems under UHV leads to the emergence of new reconstructions of the Ge(110) and Ge(111) surfaces. Thermal processing also enables strain modification of the overlying graphene lattice, with tunability afforded by the unique geometries of the different Ge crystal surfaces. This work demonstrates that the prevalence and influence of strain in the Ge/graphene system plays a significant role in dictating both the atomic structure and electronic properties of the material interface and thus will inform future work on this material system.

■ ASSOCIATED CONTENT

Supporting Information

The Supporting Information is available free of charge on the ACS Publications website at DOI: [10.1021/acs.nanolett.5b02833](https://doi.org/10.1021/acs.nanolett.5b02833).

Additional information on materials and methods, LEED data, UHV preparation of Ge surfaces, Ge(111) partial steps, graphene charge homogeneity on Ge(111), native Ge surface reconstructions, Raman mapping data, Raman reference data, Raman mode statistics, and further STM/STS of annealed graphene on Ge(001) ([PDF](#))

■ AUTHOR INFORMATION

Corresponding Authors

*E-mail: nguisinger@anl.gov.

*E-mail: m-hersam@northwestern.edu.

Notes

The authors declare no competing financial interest.

■ ACKNOWLEDGMENTS

The authors would like to thank Brandon Fisher for technical support. This work was performed, in part, at the Center for Nanoscale Materials, a U.S. Department of Energy Office of Science User Facility under Contract No. DE-AC02-06CH11357. This work was supported by the U.S. Department of Energy SISGR contract No. DE-FG02-09ER16109, the Office of Naval Research (Grant No. N00014-14-1-0669), and the National Science Foundation Graduate Fellowship DGE-0824162 and DGE-1324585. R.M.J. and M.S.A. acknowledge support from the Department of Energy (DOE) Office of Science Early Career Research Program through the Office of Basic Energy Sciences (No. DE-SC0006414) for graphene synthesis, and R.M.J. also acknowledges support from the Department of Defense (DOD) Air Force Office of Scientific Research through the National Defense Science and Engineering Graduate Fellowship (No. 32 CFR 168a). G.P.C. and M.J.B. acknowledge support from the Northwestern University MRSEC (Award No. DMR-1121262 from the National Science Foundation).

■ REFERENCES

- (1) Li, X.; Cai, W.; An, J.; Kim, S.; Nah, J.; Yang, D.; Piner, R.; Velamakanni, A.; Jung, I.; Tutuc, E. *Science* **2009**, *324*, 1312–1314.
- (2) Kim, K. S.; Zhao, Y.; Jang, H.; Lee, S. Y.; Kim, J. M.; Kim, K. S.; Ahn, J.-H.; Kim, P.; Choi, J.-Y.; Hong, B. H. *Nature* **2009**, *457*, 706–710.
- (3) Reina, A.; Jia, X.; Ho, J.; Nezich, D.; Son, H.; Bulovic, V.; Dresselhaus, M. S.; Kong, J. *Nano Lett.* **2009**, *9*, 30–35.
- (4) Geim, A. K.; Novoselov, K. S. *Nat. Mater.* **2007**, *6*, 183–191.
- (5) Kiraly, B.; Iski, E. V.; Mannix, A. J.; Fisher, B. L.; Hersam, M. C.; Guisinger, N. P. *Nat. Commun.* **2013**, *4*, 2804.
- (6) Gao, L.; Ren, W.; Xu, H.; Jin, L.; Wang, Z.; Ma, T.; Ma, L.-P.; Zhang, Z.; Fu, Q.; Peng, L.-M.; Bao, X.; Cheng, H.-M. *Nat. Commun.* **2012**, *3*, 699.
- (7) Geng, D.; Wu, B.; Guo, Y.; Huang, L.; Xue, Y.; Chen, J.; Yu, G.; Jiang, L.; Hu, W.; Liu, Y. *Proc. Natl. Acad. Sci. U. S. A.* **2012**, *109*, 7992–7996.
- (8) Sun, Z.; Yan, Z.; Yao, J.; Beitler, E.; Zhu, Y.; Tour, J. M. *Nature* **2010**, *468*, 549–552.
- (9) Wan, X.; Chen, K.; Liu, D.; Chen, J.; Miao, Q.; Xu, J. *Chem. Mater.* **2012**, *24*, 3906–3915.
- (10) Li, Z.; Wu, P.; Wang, C.; Fan, X.; Zhang, W.; Zhai, X.; Zeng, C.; Li, Z.; Yang, J.; Hou, J. *ACS Nano* **2011**, *5*, 3385–3390.
- (11) Ruan, G.; Sun, Z.; Peng, Z.; Tour, J. M. *ACS Nano* **2011**, *5*, 7601–7607.
- (12) Tsen, A. W.; Brown, L.; Levendorf, M. P.; Ghahari, F.; Huang, P. Y.; Havener, R. W.; Ruiz-Vargas, C. S.; Muller, D. A.; Kim, P.; Park, J. *Science* **2012**, *336*, 1143–1146.
- (13) Hao, Y.; Bharathi, M. S.; Wang, L.; Liu, Y.; Chen, H.; Nie, S.; Wang, X.; Chou, H.; Tan, C.; Fallahazad, B.; Ramanarayanan, H.; Magnuson, C. W.; Tutuc, E.; Yakobson, B. I.; McCarty, K. F.; Zhang, Y. W.; Kim, P.; Hone, J.; Colombo, L.; Ruoff, R. S. *Science* **2013**, *342*, 720–723.
- (14) Gao, L.; Guest, J. R.; Guisinger, N. P. *Nano Lett.* **2010**, *10*, 3512–3516.
- (15) Sutter, P. W.; Flege, J.-I.; Sutter, E. A. *Nat. Mater.* **2008**, *7*, 406–411.
- (16) Jacobberger, R. M.; Arnold, M. S. *Chem. Mater.* **2013**, *25*, 871–877.
- (17) Jacobberger, R. M.; Levesque, P. L.; Xu, F.; Wu, M.-Y.; Choubak, S.; Desjardins, P.; Martel, R.; Arnold, M. S. *J. Phys. Chem. C* **2015**, *119*, 11516–11523.
- (18) Wang, G.; Zhang, M.; Zhu, Y.; Ding, G.; Jiang, D.; Guo, Q.; Liu, S.; Xie, X.; Chu, P. K.; Di, Z.; Wang, X. *Sci. Rep.* **2013**, *3*, 2465.
- (19) Lee, J. H.; Lee, E. K.; Joo, W. J.; Jang, Y.; Kim, B. S.; Lim, J. Y.; Choi, S. H.; Ahn, S. J.; Ahn, J. R.; Park, M. H.; Yang, C. W.; Choi, B. L.; Hwang, S. W.; Whang, D. *Science* **2014**, *344*, 286–289.
- (20) Novoselov, K. S.; Geim, A. K.; Morozov, S. V.; Jiang, D.; Zhang, Y.; Dubonos, S. V.; Grigorieva, I. V.; Firsov, A. A. *Science* **2004**, *306*, 666–669.
- (21) Zhang, Y.; Tan, Y.-W.; Stormer, H. L.; Kim, P. *Nature* **2005**, *438*, 201–204.
- (22) Novoselov, K. S.; Geim, A. K.; Morozov, S. V.; Jiang, D.; Katsnelson, M. I.; Grigorieva, I. V.; Dubonos, S. V.; Firsov, A. A. *Nature* **2005**, *438*, 197–200.
- (23) Chung, T.-F.; He, R.; Wu, T.-L.; Chen, Y. P. *Nano Lett.* **2015**, *15*, 1203–1210.
- (24) Dean, C. R.; Young, A. F.; Meric, I.; Lee, C.; Wang, L.; Sorgenfrei, S.; Watanabe, K.; Taniguchi, T.; Kim, P.; Shepard, K. L. *Nat. Nanotechnol.* **2010**, *5*, 722–726.
- (25) Martin, J.; Akerman, N.; Ulbricht, G.; Lohmann, T.; Smet, J. H.; Klitzing, von, K.; Yacoby, A. *Nat. Phys.* **2008**, *4*, 144–148.
- (26) Fratini, S.; Guinea, F. *Phys. Rev. B: Condens. Matter Mater. Phys.* **2008**, *77*, 195415.
- (27) Riedl, C.; Coletti, C.; Iwasaki, T.; Zakharov, A. A.; Starke, U. *Phys. Rev. Lett.* **2009**, *103*, 246804.
- (28) Larciprete, R.; Ulstrup, S.; Lacovig, P.; Dalmiglio, M.; Bianchi, M.; Mazzola, F.; Horneker, L.; Orlando, F.; Baraldi, A.; Hofmann, P.; Lizzit, S. *ACS Nano* **2012**, *6*, 9551–9558.

- (29) Schumacher, S.; Wehling, T. O.; Lazić, P.; Runte, S.; Förster, D. F.; Busse, C.; Petrović, M.; Kralj, M.; Blügel, S.; Atodiresei, N.; Caciuc, V.; Michely, T. *Nano Lett.* **2013**, *13*, 5013–5019.
- (30) Rahnejat, K. C.; Howard, C. A.; Shuttleworth, N. E.; Schofield, S. R.; Iwaya, K.; Hirjibehedin, C. F.; Renner, C.; Aepli, G.; Ellerby, M. *Nat. Commun.* **2011**, *2*, 558.
- (31) Gorbachev, R. V.; Geim, A. K.; Katsnelson, M. I.; Novoselov, K. S.; Tudorovskiy, T.; Grigorieva, I. V.; MacDonald, A. H.; Morozov, S. V.; Watanabe, K.; Taniguchi, T.; Ponomarenko, L. A. *Nat. Phys.* **2012**, *8*, 896–901.
- (32) Ponomarenko, L. A.; Gorbachev, R. V.; Yu, G. L.; Elias, D. C.; Jalil, R.; Patel, A. A.; Mishchenko, A.; Mayorov, A. S.; Woods, C. R.; Wallbank, J. R.; Mucha-Kruczynski, M.; Piot, B. A.; Potemski, M.; Grigorieva, I. V.; Novoselov, K. S.; Guinea, F.; Fal'ko, V. I.; Geim, A. K. *Nature* **2014**, *497*, 594–597.
- (33) Dean, C. R.; Wang, L.; Maher, P.; Forsythe, C.; Ghahari, F.; Gao, Y.; Katoch, J.; Ishigami, M.; Moon, P.; Koshino, M.; Taniguchi, T.; Watanabe, K.; Shepard, K. L.; Hone, J.; Kim, P. *Nature* **2013**, *497*, 598–602.
- (34) Hunt, B.; Sanchez-Yamagishi, J. D.; Young, A. F.; Yankowitz, M.; LeRoy, B. J.; Watanabe, K.; Taniguchi, T.; Moon, P.; Koshino, M.; Jarillo-Herrero, P.; Ashoori, R. C. *Science* **2013**, *340*, 1427–1430.
- (35) Gorbachev, R. V.; Song, J. C. W.; Yu, G. L.; Kretinin, A. V.; Withers, F.; Cao, Y.; Mishchenko, A.; Grigorieva, I. V.; Novoselov, K. S.; Levitov, L. S.; Geim, A. K. *Science* **2014**, *346*, 448–451.
- (36) Pereira, V. M.; Castro Neto, A. H.; Peres, N. M. R. *Phys. Rev. B: Condens. Matter Mater. Phys.* **2009**, *80*, 045401.
- (37) Goerbig, M. O.; Fuchs, J.-N.; Montambaux, G.; Piéchon, F. *Phys. Rev. B: Condens. Matter Mater. Phys.* **2008**, *78*, 045415.
- (38) Levy, N.; Burke, S. A.; Meaker, K. L.; Panlasigui, M.; Zettl, A.; Guinea, F.; Neto, A. C.; Crommie, M. F. *Science* **2010**, *329*, 544–547.
- (39) Gomes, K. K.; Mar, W.; Ko, W.; Guinea, F.; Manoharan, H. C. *Nature* **2013**, *483*, 306–310.
- (40) Bissett, M. A.; Tsuji, M.; Ago, H. *Phys. Chem. Chem. Phys.* **2014**, *16*, 11124.
- (41) Lee, G.; Mai, H.; Chizhov, I.; Willis, R. F. *Surf. Sci.* **2000**, *463*, 55–65.
- (42) Zandvliet, H. J. W. *Phys. Rep.* **2003**, *388*, 1–40.
- (43) Ritter, K. A.; Lyding, J. W. *Nat. Mater.* **2009**, *8*, 235–242.
- (44) Rutter, G. M.; Guisinger, N. P.; Crain, J. N.; Jarvis, E. A. A.; Stiles, M. D.; Li, T.; First, P. N.; Stroscio, J. A. *Phys. Rev. B: Condens. Matter Mater. Phys.* **2007**, *76*, 235416.
- (45) Koepke, J. C.; Wood, J. D.; Estrada, D.; Ong, Z.-Y.; He, K. T.; Pop, E.; Lyding, J. W. *ACS Nano* **2013**, *7*, 75–86.
- (46) Zhang, Y.; Brar, V. W.; Girit, C.; Zettl, A.; Crommie, M. F. *Nat. Phys.* **2009**, *5*, 722–726.
- (47) Xue, J.; Sanchez-Yamagishi, J.; Bulmash, D.; Jacquod, P.; Deshpande, A.; Watanabe, K.; Taniguchi, T.; Jarillo-Herrero, P.; LeRoy, B. J. *Nat. Mater.* **2011**, *10*, 282–285.
- (48) He, K. T.; Koepke, J. C.; Barraza-Lopez, S.; Lyding, J. W. *Nano Lett.* **2010**, *10*, 3446–3452.
- (49) Decker, R.; Wang, Y.; Brar, V. W.; Regan, W.; Tsai, H.-Z.; Wu, Q.; Gannett, W.; Zettl, A.; Crommie, M. F. *Nano Lett.* **2011**, *11*, 2291–2295.
- (50) Mayorov, A. S.; Gorbachev, R. V.; Morozov, S. V.; Britnell, L.; Jalil, R.; Ponomarenko, L. A.; Blake, P.; Novoselov, K. S.; Watanabe, K.; Taniguchi, T.; Geim, A. K. *Nano Lett.* **2011**, *11*, 2396–2399.
- (51) Ahn, G.; Kim, H. R.; Ko, T. Y.; Choi, K.; Watanabe, K.; Taniguchi, T.; Hong, B. H.; Ryu, S. *ACS Nano* **2013**, *7*, 1533–1541.
- (52) Lee, J. E.; Ahn, G.; Shim, J.; Lee, Y. S.; Ryu, S. *Nat. Commun.* **2012**, *3*, 1024.
- (53) Doniach, S.; Sunjic, M. *J. Phys. C: Solid State Phys.* **1970**, *3*, 285.
- (54) van Attekum, P. M. T. M.; Wertheim, G. K. *Phys. Rev. Lett.* **1979**, *43*, 1896–1898.
- (55) Cheung, T. T. P. *J. Appl. Phys.* **1982**, *53*, 6857.